

# 1 Corollary Discharge Promotes a 2 Sustained Motor State in a Neural 3 Circuit for Navigation

4 Ni Ji<sup>1†</sup>, Vivek Venkatachalam<sup>1‡</sup>, Hillary Rodgers<sup>1,3</sup>, Wesley Hung<sup>2</sup>, Taizo Kawano<sup>2</sup>,  
5 Christopher M. Clark<sup>3</sup>, Maria Lim<sup>2</sup>, Mark J. Alkema<sup>3\*</sup>, Mei Zhen<sup>2\*</sup>, Aravinthan D.T.  
6 Samuel<sup>1\*</sup>

**\*For correspondence:**

[mark.alkema@umassmed.edu](mailto:mark.alkema@umassmed.edu)  
(MA); [zhen@lunenfeld.ca](mailto:zhen@lunenfeld.ca) (MZ);  
[samuel@physics.harvard.edu](mailto:samuel@physics.harvard.edu)  
(ADTS)

**Present address:** <sup>†</sup>Department of 10  
Brain and Cognitive Sciences, MIT,  
Cambridge, MA USA; <sup>‡</sup>Department 11  
of Physics, Northeastern University,  
Boston, MA USA

7 <sup>1</sup>Department of Physics and Center for Brain Science, Harvard University, 17 Oxford  
8 Street, Cambridge, MA 02138 USA; <sup>2</sup>Lunenfeld-Tanenbaum Research Institute, Mount  
9 Sinai Hospital, Toronto, ON, Canada M5G 1X5; and Departments of Molecular Genetics,  
and Physiology, University of Toronto, Toronto, ON, Canada M5S 1A8

---

12 **Abstract** Animals exhibit behavioral and neural responses that persist on longer time scales  
13 than transient or fluctuating stimulus inputs. Here, we report that *C. elegans* uses corollary  
14 discharge to sustain motor responses during thermotactic navigation. By imaging circuit activity in  
15 behaving animals, we show that a principal postsynaptic partner of the AFD thermosensory neuron,  
16 the AIY interneuron, encodes both temperature and motor state information. By optogenetic and  
17 genetic manipulation of this circuit, we demonstrate that the motor state representation in AIY is a  
18 corollary discharge signal. RIM, an interneuron that is connected with premotor interneurons, is  
19 required for corollary discharge. Ablation of RIM eliminates the motor representation in AIY, allows  
20 thermosensory representations to reach downstream premotor interneurons, and reduces the  
21 animal's ability to sustain forward movements during thermotaxis. We propose that corollary  
22 discharge underlies a positive feedback mechanism to generate persistent neural activity and  
23 sustained behavioral patterns in a sensorimotor transformation.

---

## 25 Introduction

26 Behavioral states often persist over longer timescales than their initiating sensory stimuli (*Bidaye*  
27 *et al., 2014; Hoopfer et al., 2015*). For example, fish continue to fixate their gaze on light after the  
28 onset of darkness (*Seung, 1996; Aksay et al., 2007*). A brief aversive stimulus evokes prolonged  
29 escape responses in many species (*Li et al., 2006; Herberholz et al., 2002*). Lasting behavioral  
30 states require circuit mechanisms to turn a transient stimulus into persistent neuronal activity  
31 (*Lee and Dan, 2012; Major and Tank, 2004*). One circuit topology that can produce persistent  
32 neural activity is positive feedback (*Seung, 1996*). However, establishing causality between positive  
33 feedback, persistent neural activity, and sustained behavior states has been challenging because of  
34 the technical difficulties in experimentally dissecting neural activities across entire sensorimotor  
35 pathways.

36 The compact nervous system and optical accessibility of *C. elegans* make it possible to explore  
37 molecular and circuit mechanisms that underlie persistent neural activities and sustained behavioral  
38 states in intact animals (*Gao et al., 2015*). *C. elegans* requires persistent motor states to navigate  
39 variable sensory environments. During locomotion, the animal alternates between sustained  
40 forward movements and short reversals. When navigating through a chemical or thermal gradient,

41 *C. elegans* exhibits biased random walks, extending forward runs towards preferred environments  
42 (Pierce-Shimomura et al., 1999; Ryu and Samuel, 2002; Ino and Yoshida, 2009). *C. elegans* can also  
43 exhibit klinotaxis, the gradual steering of heading angles during forward movements towards  
44 preferred directions (Ward, 1973; Ino and Yoshida, 2009). *C. elegans* employs both biased random  
45 walk and head steering (Hedgecock and Russell, 1975; Mori and Ohshima, 1995; Luo et al., 2014a)  
46 to actively move up or down a temperature gradient towards preferred temperatures – positive or  
47 negative thermotaxis, respectively.

48 The *C. elegans* wiring diagram has a layered organization (White et al., 1986) (Figure 2B). Sensory  
49 neurons communicate with first layer interneurons. Second layer interneurons communicate  
50 with head motor neurons and premotor interneurons that regulate body undulation. AFD is  
51 the thermosensory neuron that mediates both positive and negative thermotaxis (Luo et al.,  
52 2014a; Hawk et al., 2018). Its principal chemical synaptic partner, AIY, is the first layer interneuron  
53 specifically required for positive thermotaxis. Inactivation or ablation of AIY causes animals to  
54 exhibit negative thermotaxis at all temperatures (Mori and Ohshima, 1995; Hobert et al., 1997).

55 AIY responds to temperature variations due to signaling from AFD (Clark et al., 2006; Narayan  
56 et al., 2011; Hawk et al., 2018). Excitatory synapses from AFD to AIY reliably transmit AFD's activity  
57 pattern into scaled AIY dynamics (Narayan et al., 2011). AIY is postsynaptic to multiple sensory  
58 neurons, and is thought to play a role in navigation across different sensory modalities by controlling  
59 the duration of forward runs (Gray et al., 2005; Wakabayashi et al., 2004; Tsalik and Hobert, 2003).  
60 AIY has also been shown to regulate the speed and direction of locomotion (Li et al., 2014; Kocabas  
61 et al., 2012).

62 We probed mechanisms by which AIY biases random walks during positive thermotaxis. Our  
63 calcium imaging of AIY in moving animals reveals that AIY encodes both temperature and motor  
64 information. Consistent with a previous report (Luo et al., 2014b), we show that AIY activity rises at  
65 the onset of forward runs and falls at the onset of reversals. But we further reveal that whether AIY  
66 encodes the thermosensory input from the AFD neuron depends on motor state. During forward  
67 runs, AIY activity follows AFD activity, rising during warming and falling during cooling. During  
68 reversals, AIY does not encode AFD thermosensory input. We demonstrate that the motor state  
69 representation in AIY reflects corollary discharge (CD), a copy of the motor command. Corollary  
70 discharge to AIY requires RIM, an interneuron that is connected with both the forward and reversal  
71 premotor circuit. In the absence of RIM, AIY encodes thermosensory input from AFD regardless  
72 of motor state. Moreover, weak thermosensory representations appeared in some premotor  
73 interneurons. At the behavioral level, absence of RIM causes positive thermotaxis to be disrupted  
74 by reduced ability to sustain forward movement up temperature gradients. These experimental  
75 results support a minimal phenomenological model where both warming and corollary discharge  
76 reinforce and sustain the forward motor state in a biased random walk. Therefore, in *C. elegans*,  
77 motor state shapes sensory processing by feedback from premotor interneurons to first layer  
78 interneurons. Our results establish a role for corollary discharge in sustaining a motor state despite  
79 variable or fluctuating sensory environments.

## 80 Results

### 81 Sustained forward movements across thermal fluctuations in positive thermotaxis

82 *C. elegans* navigates towards temperatures that correspond to prior thermal experience. To evoke  
83 positive thermotaxis, we placed young adults cultivated at 25°C on a linear thermal gradient span-  
84 ning 19 to 23°C (Figure 1). Consistent with earlier reports, these animals exhibited biased random  
85 walk and klinotaxis towards warmer temperatures (Figure 1B) ((Luo et al., 2014a; Yamaguchi et al.,  
86 2018): runs that pointed in favorable directions were lengthened (Figure 1B; forward heading  
87 angles gradually reoriented towards temperatures that correspond to prior experience (Figure 1B).  
88 Without a temperature gradient, there was no evident modulation of either run length or heading  
89 angle (Figure 1B).

90 Individual trajectories during positive thermotaxis revealed periods of forward movement that  
91 carry the animal up the temperature gradient. Although these periods of forward movement are  
92 persistent in duration, they are not always persistent in direction (**Figure 1C**). *C. elegans* experiences  
93 temporal changes in temperature on spatial gradients because of its own movements. Because of  
94 changes in movement direction, most runs – even those that orient the animal towards warmer  
95 temperatures – will typically involve detection of both warming and cooling stimuli (**Figure 1D**). Thus,  
96 *C. elegans* has an ability to sustain forward movement up temperature gradients across transient  
97 cooling fluctuations.

### 98 **Thermosensory encoding in AIY depends on motor state**

99 We sought circuit mechanisms for sustaining forward movement up temperature gradients despite  
100 thermal fluctuations.

101 First, we measured the activity of the AFD thermosensory neuron and AIY, its principle postsy-  
102 naptic partner, by calcium imaging in moving animals. Subjected to oscillating temperatures below  
103 the preferred temperature, *C. elegans* exhibits positive thermotaxis. As previously reported (**Clark**  
104 **et al., 2006, 2007**), AFD's activity phase locks to periodic variations in temperatures, rising upon  
105 warming and falling upon cooling (**Figure 2A**). The power spectrum of AFD activity shows a strong  
106 peak corresponding to the frequency of thermal oscillation (**Figure 2A**). AFD activity showed no  
107 strong correlation with the motor state (**Figure 2**) (Spearman's  $\rho < 0.1$ ,  $N = 6$ ), indicating that motor  
108 commands arise downstream of the thermosensory neuron.

109 To understand the activity patterns of AIY, we simultaneously monitored AIY calcium dynamics  
110 along with components of the motor circuit known to code forward and reversal motor states  
111 (**Figure 2B,C**). We found that AIY encodes both motor and temperature information. During forward  
112 movements, AIY's calcium activity phase locked to temperature changes, increasing upon warming  
113 and decreasing upon cooling (**Figure 2D**). This response was attenuated during reversals (**Figure 2D**).  
114 As a result, the frequency of temperature oscillations is less well represented in the power spectrum  
115 of AIY activity than that of AFD ( $p < 0.01$ , Wilcoxon rank-sum test;  $N = 6$ ) (**Figure 2D**).

116 Unlike AFD and AIY, all motor circuit neurons that we examined strictly encode motor information  
117 during thermosensory stimulation. The AVA premotor interneuron is active during and regulates  
118 backward movement (**Chalfie et al., 1985; Kawano et al., 2011; McCormick et al., 2011; Kato et al.,**  
119 **2015**) (**Figure 2B**). In animals subjected to oscillating thermosensory stimulation, AVA calcium  
120 activity exhibited high and low states that correlated with backward and forward movement,  
121 respectively (**Figure 2D**). We detected no representation of the stimulus frequency in the power  
122 spectrum of AVA's activity pattern ( $p > 0.1$ , Wilcoxon rank-sum test,  $N = 5$ , **Figure 2D**). Similarly, during  
123 thermosensory stimulation, the RME and SMD head motor neurons exhibited both high and low  
124 states that coincided with animal's directional movements (**Figure 2D**), as reported in previous  
125 studies (**Hendricks, 2012**). The power spectra of RME and SMD activity patterns also revealed no  
126 representation of thermosensory input (**Figure 2D**).

127 For positive thermotaxis, the sensorimotor transformation progresses through three layers  
128 (**Figure 2B**): the first layer encodes only thermal stimuli; the first layer interneuron encodes both  
129 thermal stimuli and motor states; the premotor and motor layer encode only motor states.

### 130 **Motor coding in AIY is a corollary discharge signal that requires the RIM interneuron**

131 Our finding that AIY encodes thermal information in a manner that depends on motor state suggests  
132 a critical role in sensorimotor transformations during positive thermotaxis. In animals exposed  
133 to either constant or oscillating temperatures, AIY activity consistently rises at the beginning of  
134 forward runs and decays at the onset of reversals (**Figure 3**). How does AIY, a first order interneuron,  
135 acquire a motor signal?  
136

137 We explored the possibility that proprioception, elicited by movement itself, underlies the  
138 calcium response in AIY. We imaged the thermosensory circuit activity in immobilized animals

139 subjected to constant temperature. As in moving animals, AIY's activity remained anti-correlated  
140 with neurons active during reversals (AVA) and correlated with neurons active during forward  
141 movement (RME and SMDD/V) (**Figure 2–Figure Supplement 1**). *C. elegans* movement is not required  
142 for AIY activity to reflect motor state, arguing against proprioception.

143 We also tested whether motor commands are generated by AIY and transmitted to the premotor  
144 and motor circuits. We imaged AIY's activity upon blocking its chemical synaptic transmission by  
145 AIY-specific expression of tetanus toxin (TeTx) (**Figure 3B**). Without chemical synaptic output, AIY  
146 activity remained strongly coupled to the motor state, implying that AIY must receive the motor  
147 state signal.

148 We asked whether AIY receives corollary discharge from neurons that encode the motor com-  
149 mand. We imaged AIY activity in moving animals upon ablation of AIY's downstream interneurons  
150 and premotor interneurons (**Figure 4A**). For interneurons, we focused on AIB and RIM. AIB shares  
151 electrical synapses with RIM and the AFD thermosensory neuron (**White et al., 1986**). In the context  
152 of chemotaxis, AIB and RIM have been shown to regulate variability in the neuronal and behav-  
153 ioral response to olfactory inputs (**Gordus et al., 2015**). We also tested AVA and AVB, premotor  
154 interneurons that regulate reversal and forward movement, respectively. Ablations were performed  
155 by expressing flavoprotein miniSOG, which induces acute functional loss and neuronal death by  
156 photoactivation (**Qi et al., 2012**).

157 We found that ablating AIB did not remove the motor state representation in AIY (**Figure 4B, D**).  
158 Neither did the removal of the premotor interneurons AVA or AVB alone (**Figure 4B**). However, AIY  
159 lost its motor state representation when we ablated RIM, either by itself or in combination with  
160 other premotor interneurons (**Figure 4B, C**).

161 RIM activity has been shown to be correlated with the AVA premotor interneuron that promotes  
162 reversals and anti-correlated with the AVB premotor interneuron that promotes forward movement  
163 (**Kawano et al., 2011**). To further probe whether RIM is required for the motor state signal to appear  
164 in AIY, we optogenetically activated either AVA or AVB while simultaneously measuring AIY calcium  
165 activity in immobilized animals. Activation of AVA using the light-gated opsin chrimson (**Klapoetke  
166 et al., 2014**) triggered a decrease in AIY calcium levels. Activation of AVB triggered an increase in  
167 AIY calcium levels (**Figure 4E**). When RIM was ablated, AIY calcium signals no longer responded to  
168 optogenetic activation of either AVA or AVB, suggesting that RIM is part of the CD pathway from the  
169 motor circuit to AIY. Without RIM, AIY activity no longer reflected or depended on the motor state,  
170 but the premotor interneurons AVA and head motor neurons RME and RMD continued to encode  
171 for the backward and forward movement, albeit with reduced bimodal activity (**Figure 5A,B**). Thus,  
172 RIM is not essential for generating motor commands, but is necessary to relay motor information  
173 to AIY, a first layer interneuron.

### 174 **RIM-mediated corollary discharge does not depend on chemical synaptic transmis-** 175 **sion**

176 We sought synaptic mechanisms by which RIM may contribute to the CD pathway. RIM expresses  
177 VGLUT3/EAT-4, indicating the potential involvement of glutamatergic synaptic transmission. RIM  
178 also synthesizes tyramine (**Serrano-Saiz et al., 2013**), a monoamine neuromodulator (**Alkema et al.,  
179 2005**). We imaged AIY activity in loss-of-function mutants for glutamatergic signaling (**VGLUT3/eat-  
180 4**), tyramine synthesis (**TDC/tdc-1**), vesicular monoamine transport (**VMAT/cat-1**) and peptidergic  
181 signaling (**CAPS/unc-31**). We found that AIY activity remained coupled to motor state in all mutants,  
182 but the difference in AIY activity between the backward and forward states was less distinct in  
183 mutants defective for vesicular monoamine transport (**VMAT/cat-1**) or tyramine synthesis (**TDC/tdc-1**)  
184 (**Figure 5C,D**). This effect was similar to when we blocked RIM neurotransmitter release by TeTx  
185 (**Ptdc-1::TeTx**) (**Figure 5C,D**).

186 Since perturbation of chemical synaptic transmission did not abolish motor-related activity in  
187 AIY, neuronal communication that is independent of classic chemical synaptic transmission plays  
188 roles in relaying corollary discharge to AIY. As previously reported (**Kawano et al., 2011; Kato et al.,**

189 **2015; Gordus et al., 2015**), RIM activity is strongly correlated with the AVA premotor interneuron,  
190 higher during reversals and lower during forward movement. AIY, on the other hand, exhibits  
191 increased activity during forward movement (**Figure 3**). Therefore, the corollary discharge signal  
192 must undergo sign reversal when propagated from RIM to AIY. Our observations suggest that the  
193 joint representation of sensory and motor signals in AIY arises from separate sources: feedforward  
194 input from AFD and feedback from the motor circuit that is conveyed through RIM.

### 195 **A role for RIM-dependent corollary discharge during positive thermotaxis**

196 RIM plays a critical role in the motor state dependent modulation of AIY calcium activity. This  
197 prompted us to examine the effect of disrupting the CD signal on sensorimotor transformations  
198 in behaving animals. When RIM-ablated animals were subjected to oscillating temperatures,  
199 AIY activity was no longer coupled to the motor state, but instead reliably tracked temperature  
200 fluctuations during both forward and backward movements (**Figure 6**). The stronger representation  
201 of an oscillating temperature in AIY activity was evident in its power spectrum (**Figure 6A, B**;  $p < 0.001$   
202 Wilcoxon rank sum test). When RIM was ablated, we were also able to detect the representation  
203 of thermosensory oscillations in the activity pattern of the AVA premotor interneuron and the  
204 SMDD head motor neuron (**Figure 6**). This observation suggests that the loss of the RIM-dependent  
205 CD signal resulted in a sensorimotor circuit that becomes more susceptible to fluctuations in  
206 thermosensory input. Without RIM and the CD signal to AIY, thermosensory representations of  
207 fluctuating inputs can reach the motor circuit. The CD signal may thus play an important role in  
208 sustaining motor outputs across rapidly varying sensory inputs.

209 We tested this hypothesis by examining the effect of RIM ablation on positive thermotaxis  
210 (**Figure 6D**). These animals were specifically defective in their ability to sustain forward locomotion  
211 when moving up the thermal gradient (**Figure 6E**). The gradual heading angle reorientation during a  
212 forward run remained intact (**Figure 6F**). Thus, the thermotaxis defect of RIM ablated animals is a  
213 disruption in the ability to sustain forward runs up temperature gradients.

### 214 **Agent-based simulations driven by a reduced model recapitulate the role of CD 215 feedback in positive thermotaxis**

216 To illustrate how corollary discharge could contribute to sustained motor states during thermotaxis,  
217 we built a minimal phenomenological model of the thermotaxis circuit (**Figure 7**). In this model,  
218 temperature fluctuations encoded by a thermosensory neuron is conveyed to a downstream  
219 interneuron. The interneuron outputs to a motor command circuit that determines the motor state.  
220 A copy of the motor command is relayed back to the interneuron in a manner that reinforces the  
221 ongoing motor state, effectively forming a positive feedback loop. When exposed to fluctuating  
222 inputs, this circuit transitioned between two stable states at time scales much longer than the input  
223 signal (**Figure 7B**).

224 We used this circuit model to simulate animal locomotion along linear thermal gradients (**Fig-  
225 ure 7C**). The model with strong corollary discharge most effectively drove migration up the tempera-  
226 ture gradient. In this case, forward runs up the temperature gradient were substantially longer than  
227 those down the gradient (**Figure 7D,E**). Decreasing the strength of corollary discharge lessened the  
228 dependence of run length on run direction, and led to less efficient and less reliable thermotaxis  
229 (**Figure 7C, D, E**).

## 230 **Discussion**

231 Positive feedback as a circuit topology has been proposed to sustain neural activity patterns (**Seung,  
232 1996; Major and Tank, 2004**). Here, we uncovered a role for corollary discharge, a feedback signal  
233 from the motor circuit, in sustaining a neural state for forward locomotion. By relaying a motor  
234 command to a first layer interneuron in the sensorimotor pathway, this circuitry couples warming  
235 signals with forward motor state signals. These signals reinforce each other, leading to sustained

236 periods of forward movement up temperature gradients. Sustained neural activity states allow the  
237 animal to filter rapid fluctuations in sensory input from affecting motor behavior, thereby enabling  
238 persistent behavioral outputs.

239 Emerging evidence from across species indicates that motor states can significantly impact  
240 sensory processing (Seelig and Jayaraman, 2015; Fu et al., 2014; Schneider et al., 2014; Zagha et al.,  
241 2013; Petreanu et al., 2009; Ouellette et al., 2018). An explicit dependence of sensory encoding on  
242 behavioral states may contribute to observed variability in stimulus-evoked behavioral responses.  
243 In *C. elegans* chemotaxis, variability in neuronal and behavioral responses has been linked to the RIM  
244 interneuron. The AWC olfactory neuron reliably responds to olfactory inputs, but its downstream  
245 partner, the AIB interneuron, responds less reliably. Ablation of RIM reduces the variability in the  
246 AIB response. One interpretation of the role of RIM in the olfactory circuit is that it enhances the  
247 variability of a probabilistic sensorimotor transformation during the biased random walk towards  
248 chemoattractants (Gordus et al., 2015). By studying the circuit in moving animals, our results  
249 favor the interpretation for a different role for RIM. During thermotaxis, RIM allows AIY, a first-layer  
250 interneuron, to generate response variability that is not stochastic but directly correlated with motor  
251 state. This observation underscores the importance of measuring sensorimotor transformations in  
252 behaving animals where feedback loops are active.

253 The motor state signal in the AIY interneuron requires the RIM interneuron. We do not know  
254 the synaptic mechanism by which the corollary discharge reaches AIY. One possibility is that it  
255 employs synaptic transmission-independent mechanisms and/or indirect feedback circuits from  
256 RIM to AIY. More extensive molecular and cellular dissection is needed to understand how the  
257 corollary discharge signal reaches AIY (Figure 2). Ablation of RIM not only eliminates the motor  
258 state representation in AIY, but also leads to increased thermosensory representation in the  
259 activity patterns of downstream neurons. Thus, the positive feedback provided to the first layer  
260 interneuron contributes to the separation of sensory input patterns in sensory neurons from motor  
261 output patterns in premotor interneurons. Behaviorally, it enhances the stability of a motor state  
262 that carries the animal up temperature gradients during positive thermotaxis, an interpretation  
263 supported by agent-based modeling (Figure 7).

264 In conclusion, our findings reveal a new role for corollary discharge. In *C. elegans* thermotaxis,  
265 corollary discharge promotes sustained neural responses to thermal stimuli and stabilizes a motor  
266 state, enhancing the efficiency of thermotactic navigation.

## 267 **Methods and Materials**

### 268 **Molecular biology and transgenic strain construction**

#### 269 Promoters

270 The following promoters were used to allow neuron-specific expression of a calcium sensor, chrim-  
271 son, and miniSOG. Most were generated from genomic DNA isolated from mixed stage N2 animals.  
272 Promoters include 4.8 kb (*Prig-3*), 0.9 kb (*Pinx-1*), 5.3 kb (*Pglr-1*), 2.9 kb (*Pcex-1*), 0.86 kb (*Plgc-55B*),  
273 3.1 kb (*Pnmr-1*) genomic sequence. All promoters except *Pnmr-1* and *Plgc-55B* used the genomic  
274 sequence of the respective length starting immediately upstream of the predicted ATG start codon  
275 of the respective genes. For *Pnmr-1*, a 2 kb internal fragment which reduces the 5.1kb *nmr-1*  
276 reporter expression was removed (Kawano et al., 2011). Details on *Plgc-55B* can be found in (Gao  
277 et al., 2015).

#### 278 Calcium imaging

279 For AIY calcium imaging, *aeals003* was generated by integrating *olaEx1621* [*Pmod-1::GCaMP6s*; *Pttx-3::RFP*;  
280 *Punc-122::mCherry*]. The integrant was outcrossed against N2 for 4 times to generate strain  
281 ADS003, and crossed into *lite-1* to generate QW1410.

282 For AFD calcium imaging, *aeals004* was generated by integrating an existing Ex line [*Pgcy-8::GCaMP6s*;  
283 *Pgcy-8::RFP*; *Punc-122::mCherry*]. The integrant was outcrossed against N2 for 4 times to  
284 generate strain ADS004.

285 For premotor interneuron and motor neuron calcium imaging, pJH3338 was constructed for  
286 calcium imaging for premotor interneurons and head motor neurons. The GCaMP6s reporter  
287 was optimized for *C. elegans* and contained three *C. elegans* introns (Lim et al., 2016; Chen et al.,  
288 2013). GCaMP6s was fused with codon-optimized mCherry (wCherry) at the C-terminus to facilitate  
289 ratiometric measurement via simultaneous imaging of GFP and RFP. The reporter expression was  
290 driven by *Pglr-1* as described above. This construct was co-injected with *lin-15(+)* marker to *lin-*  
291 *15(n765)* animals to generate extrachromosomal transgenic array *hpEx3550*, and subsequently  
292 integrated to generate *hpls471*. The integrated array was outcrossed against N2 wild-type 4 times to  
293 generate ZM8558. For simultaneous AIY and premotor/interneuron imaging, *hpls471* was crossed  
294 with *aeals003* to generate ADS027.

## 295 Neuron ablation

296 pJH2829, pJH3311, pJH2931, pJH2890, and pJH2827 were constructed for LED-based neuronal  
297 ablation for RIM, AIB, AVA (plus other neurons), AVB (plus other neurons), and AVA/AVE/AVD/RIM/PVC  
298 (plus other neurons), respectively. miniSOG fused with an outer mitochondrial membrane tag  
299 TOMM20 (tomm20-miniSOG or mito-miniSOG) (Qi et al., 2012; Shu et al., 2011). An inter-cistronic  
300 sequence splice leader (SL2) was inserted between the coding sequence of tomm20-miniSOG and  
301 codon-optimized mCherry (wCherry; a gift of A. Desai, UCSD) to visualize neurons that express  
302 miniSOG, and to examine the efficacy of ablation. SL2 sequence was PCR amplified off the splice  
303 leader sequence (SL2) between *gpd-2* and *gpd-3*. These constructs were co-injected with the *lin-15(+)*  
304 marker in *lin-15(n765)* animals to generate extrachromosomal arrays *hpEx2997*, *hpEx3464*, *hpEx3072*,  
305 *hpEx3064*, and *hpEx2940*, respectively. With the exception of *hpEx3072*, other arrays were integrated  
306 to generate *hpls327*, *hpls465*, *hpls331*, and *hpls321*. All integrated transgenic arrays were outcrossed  
307 4 times against N2, except *hpls327*, which was outcrossed 7 times against N2, before being used for  
308 behavioral analyses or to be combined with AIY calcium imaging analyses, or, behavioral analyses.

## 309 AIY imaging upon neuronal ablation

310 *aeals003* was crossed with *hpls327*, *hpls321*, *hpEx3072*, *hpls331*, and *hpls465*, respectively, to generate  
311 ADS010, ADS014, ADS026, ADS036 and ADS046. They were used for AIY calcium imaging upon  
312 ablation of RIM, premotor interneurons (with a few other neurons), and AIB, respectively.

## 313 AIY calcium imaging upon genetic manipulation of synaptic transmission and optogenetic 314 stimulation

315 For AIY imaging in genetic synaptic transmission mutants, QW1408, QW1409, QW1411, QW1175,  
316 and QW1415 were generated by crossing *aeals003* into the corresponding mutant backgrounds  
317 listed in Supplemental Table 1.

318 For AIY imaging upon cell-type specific manipulation of synaptic transmission, *aeals003* was  
319 crossed with *yxIs25*, *xuEx1414*, and *kyEx4962* to generate ADS043, ADS042, and ADS013, respectively  
320 (Li et al., 2014; Zhang et al., 2005; Gordus et al., 2015).

321 Chrimson (Klapoetke et al., 2014) was codon-optimized and fused at C-terminus with wCherry  
322 as described (Lim et al., 2016). Chrimson expression was driven by *P<sub>lgc-55B</sub>* and *Prig-3* to generate  
323 *pHR2* and *pHR6*. These constructs were co-injected with *P<sub>ges-1::GFP</sub>* into QW1410 to generate  
324 *aeaEx003* (ADS29) and *aeaEx005* (ADS31), for AIY imaging upon optogenetic stimulation of AVB and  
325 AVA, respectively.

326 *aeaEx003* and *aeaEx005* were then crossed into *hpls327;aeals003;lite-1* to generate ADS033 and  
327 ADS035 for AIY calcium imaging in RIM ablated animals, upon AVB and AVA stimulation, respectively.

## 328 Behavioral assays

### 329 Positive thermotaxis assay

330 L4 animals were cultivated at 25°C the night before the assay. On the day of the experiment, the  
331 behavioral arena was allowed to equilibrate until a stable linear thermal gradient spanning 19°C to

332 23°C was established. Before each assay session, a thin layer of NGM agar sized 20 cm on each side  
333 was placed on the arena and allowed to equilibrate to the temperature of the arena. Twenty young  
334 adults were collected from their cultivation plates and briefly washed in NGM buffer before they  
335 were transferred onto the thin agar. These animals were allowed to explore the assay environment  
336 for 5 minutes before behavioral recording starts. Afterwards, a CMOS camera positioned above  
337 the arena recorded continuously every 500 milliseconds for 20 minutes. Animal trajectories were  
338 extracted from the raw behavioral recordings using custom-written LABVIEW software. Subsequent  
339 analyses were performed in MATLAB.

#### 340 Spontaneous locomotion assay

341 Animals were cultivated and prepared for behavioral assay in identical manners as for the positive  
342 thermotaxis assay. The same behavioral arena, equilibrate to room temperature (22°C), was used  
343 to assay spontaneous locomotion. Behavioral recordings were conducted the same way as in  
344 the positive thermotaxis assay. Subsequent analyses were performed using the same LABVIEW  
345 software as above and subsequently in MATLAB.

#### 346 Calculation of thermotactic bias

347 For each animal, the instantaneous velocity ( $v$ ) and speed ( $|v|$ ) were calculated from the animal's  
348 centroid positions. The velocity vector was then projected onto direction of the thermal gradient,  
349 which in this case was parallel to the negative direction of the x-axis of the behavior arena. The  
350 thermotactic bias as the ratio between the velocity projection along the thermal gradient and the  
351 instantaneous speed of the animal:

$$352 \text{thermotactic bias} = \frac{-v_x}{|v|}$$

#### 353 Calcium imaging

##### 354 Sample preparation and imaging setup

355 L4 larval animals expressing cytosolic GCaMP6s::wCherry were cultivated at 25°C the night before  
356 the imaging experiment. Immediately before the imaging session, animals were transferred to a  
357 microscope slide with a 5% agarose pad (2 mm thick). A small drop of NGM buffer was added  
358 to the agarose pad and a # 1 coverslip was lowered onto the pad where animals could execute  
359 forward runs and reversals in a restricted area. Calcium imaging was performed on an upright  
360 spinning disc confocal microscope (Nikon Eclipse LV100 and Yokogawa CSU22) and iXon3 DU-897  
361 EMCCD camera (Andor). High resolution images were collected through a 40x, 0.95 NA Nikon Plan  
362 Apo lambda objective. 3D volumetric stacks were acquired in both the green (GCaMP6s) and red  
363 (wCherry) channels with an exposure of 30 ms at approximately 1.2 volumes per second.

##### 364 Control of thermal stimulation

365 Animals were imaged on a custom-built temperature control stage where a PID controller and  
366 H-bridge amplifier (Accuthermo) drove a thermoelectric cooler (TEC) (Newark) that pumped heat  
367 into and out of a thin copper plate with a liquid-cooled water block (Swiftech) acting as a ther-  
368 mal reservoir. A type-T thermocouple microprobe (Physitemp) was placed on the copper plate  
369 underneath a thin steel tab. A custom written Labview program was used to specify the desired  
370 temperature waveform.

##### 371 Extraction of calcium transient levels

372 To extract fluorescence intensities for individual neurons, we identified connected regions above a  
373 predefined intensity threshold and registered these regions of interest across a movie based on  
374 spatial proximity across frames. The activity level of each neuron was defined by  $\Delta R(t)/R_0$  where  
375  $R(t)$  is the ratio between the GCaMP6s intensity and the wCherry intensity at time point  $t$ , and  $R_0$  is  
376 defined as the median of the lowest ten  $R(t)$  values in the time series.

377 Optogenetic stimulation and simultaneous calcium imaging  
378 Experimental animals expressing Chrimson were grown on NGM plates supplied with 5  $\mu\text{M}$  all-trans  
379 retinal (ATR) mixed with OP50 bacteria. Control animals of the same genotypes were grown on  
380 NGM plates seeded with OP50 without ATR. The day before the experiment, L4 animals were picked  
381 onto fresh plates (with ATR for the experimental groups and without ATR for the control groups). On  
382 the day of the experiment, young adult animals were prepared for imaging in the semi-constrained  
383 preparation as described above. During imaging, pulses of red light were delivered from a filtered  
384 white LED lamp. Pulse timing was controlled by MATLAB scripts. For calcium imaging, animals were  
385 illuminated with only the blue laser (488 nm) to avoid strong activation of Chrimson.

### 386 Neuron ablation

387 Transgenic animals expressing miniSOG were collected from late L1 to L2 stage onto a small NGM  
388 plate (3.5 cm diameter). The plate was placed under a blue LED spotlight (Mightex, peak wavelength  
389 617 nm) for 40 minutes. Following illumination, the animals were allowed to recover for overnight at  
390 15°C to examine the disappearance of cells. All ablation was performed using animals that carried  
391 integrated miniSOG transgens, with the exception for AVA ablation. Ablation of AVA was carried out  
392 in animals that carried an extrachromosomal array for *Prig-3-miniSOG-SL2-RFP*, which was subjected  
393 to random loss during somatic division. Animals used for ablation were selected for those that did  
394 not show expression (hence ablation) in a pharyngeal neuron that affects the survival of ablated  
395 animals.

## 396 Statistical analysis

### 397 Statistical tests

398 The Wilcoxon rank-sum test were used in the following comparisons: 1) comparing calcium activity  
399 upon the initiation of forward runs or reversals between wild type animals and various neuron-  
400 ablation experiments, 2) comparing the probability of change in AIY activity upon the initiation of  
401 forward run or reversals between wild type and AIY::TeTX animals, 3) comparing the thermotactic  
402 bias between wild type and RIM ablated animals. To control for multiple comparison, p values were  
403 adjusted using the Benjamini-Hochberg correction. 95% confidence intervals were determined by  
404 bootstrapping.

405 Power spectral density for each calcium activity time series was estimated by first subtracting  
406 the mean of the time series, then applying Fourier transform using the `fft` function in MATLAB, and  
407 taking the square of the resulting values.

408 The bimodality coefficient (BC) was calculated as:

$$409 \quad BC = \frac{m_3^2 + 1}{m_4 + 3 \times \frac{(n-1)^2}{(n-2)(n-3)}}$$

410 where  $m_3$  is the skewness of the distribution,  $m_4$  is the excess kurtosis, and  $n$  the sample size.  
411  $BC > 0.555$  is typically taken to indicate bimodality (Pfister *et al.*, 2013).

## 412 Modeling of circuit activity and behavior

### 413 Neural circuit model

414 We use a reduced model to capture the interaction between the three key components of the  
415 thermotaxis circuit:  $V_1(t)$ , the activity of the AFD thermosensory neuron;  $V_2(t)$ , the activity of the AIY  
416 interneuron;  $V_3(t)$ , motor circuit activity. A leaky integrator model that captures the dynamics of  
417 these interconnected circuits (Figure 7A) is given by a set of coupled equations:

$$\tau_1 \frac{dV_1}{dt} = -g_{L1} (V_1 - V_{L1}) - V_{stim} \quad (1)$$

$$\tau_2 \frac{dV_2}{dt} = -g_{L2} (V_2 - V_{L2}) + F_{21}V_1 + F_{23}V_3 \quad (2)$$

$$\tau_3 \frac{dV_3}{dt} = -g_{L3} (V_3 - V_{L3}) + F_{32} V_2 \quad (3)$$

418 where  $g_{L1}$ ,  $g_{L2}$ , and  $g_{L3}$  denote non-negative leak conductances and  $V_{L1}$ ,  $V_{L2}$ , and  $V_{L3}$  denote resting  
 419 potentials. Synaptic interactions between neurons are modeled as sigmoidal functions, based on  
 420 measurements in a related nematode species (*Ferrée et al., 1999*):

$$F_{21}(V_1) = -\bar{g}_1 \left( \frac{1}{1 + \exp -k_1 * (V_1 - \beta_1)} \right) \quad (4)$$

$$F_{23}(V_3) = -\bar{g}_2 \left( \frac{1}{1 + \exp -k_2 * (V_3 - \beta_3)} \right) \quad (5)$$

$$F_{32}(V_2) = -\bar{g}_3 \left( \frac{1}{1 + \exp -k_3 * (V_2 - \beta_2)} \right) \quad (6)$$

421 where  $g_i$ ,  $k_i$ ,  $\beta_i$  define the height, steepness and inflection point of each sigmoidal function.

422 Previous studies have shown that, at temperatures close to the prior cultivation temperature,  
 423 AFD activity reliably reports the temporal derivative of the ambient temperature. To simplify the  
 424 model and focus on the role of positive feedback in the circuit, we approximated AFD activity by its  
 425 steady state value:

$$V_1(t) \cong V_{1\infty} = V_{L1} + \frac{V_{stim}}{g_{L1}} = V_{L1} + \alpha \frac{dT}{dt} \quad (7)$$

426 Substituting *Equation 7* into *Equation 2* reduces the model to two dimensions:

$$\tau_2 \frac{dV_2}{dt} = -g_{L2} V_2 + \alpha \frac{dT}{dt} + F_{23}(V_3) + C_2 \quad (8)$$

$$\tau_M \frac{dV_3}{dt} = -g_{L3} V_3 + F_{32}(V_2) + C_3 \quad (9)$$

427 where  $C_2 = g_{L2} V_{L2} + V_{L1}$  and  $C_3 = g_{L3} V_{L3}$ .

428 Numerical integration of the governing equations was used to generate the simulations shown  
 429 in *Figure 7*.

### 430 Simulation of thermotaxis behavior

431 To simulate behavior, we model the locomotory state of the animal,  $S$ , as a function of the net  
 432 activity of the motor circuit:

$$S(t) = \text{sgn}(V_3(t)) \quad (10)$$

433 where  $S(t) \geq 0$  is defined as the forward run state and  $S(t) < 0$  is defined as the reversal state.

434 During an ongoing forward run or reversal, the heading direction,  $\theta(t)$ , remains constant. At the  
 435 start of each forward run, the new heading direction is chosen randomly from a uniform distribution  
 436 with range  $0 - \pm 180^\circ$ . When a forward run ends and a reversal state starts, the heading direction  
 437 changes by  $180^\circ$ :

$$\theta(t) = \begin{cases} (\cos \theta_0, \sin \theta_0) & t = 0 \\ \theta(t - dt) & S(t) = S(t - dt) \\ -\theta(t - dt) & S(t) = 1 \text{ and } S(t - dt) = -1 \\ \cos \theta_0, \sin \theta_0 & S(t) = -1 \text{ and } S(t - dt) = 1 \end{cases} \quad (11)$$

438 To isolate the effect of corollary discharge on the duration of behavioral states, all animals are  
 439 simulated to move at constant speed (1 unit length per time step).

440 The stimulus environment is also chosen to simulate experimental conditions. A linear thermal  
 441 gradient along the  $x$  direction is set by  $T(x) = c_T x$ .

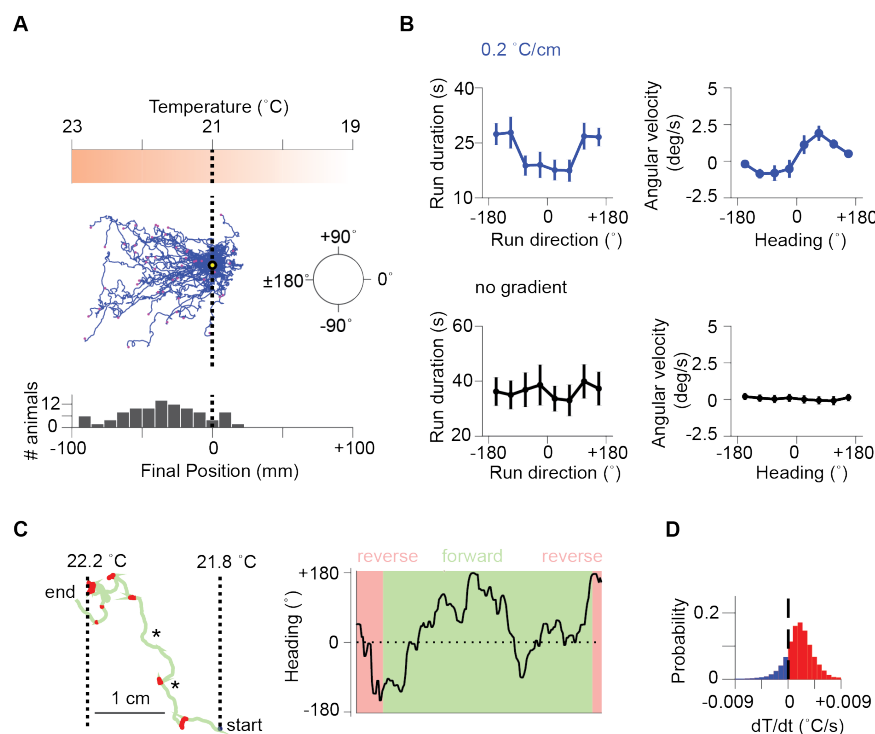


**Figure 1. Sustained forward motor state despite of temperature fluctuations during positive thermotaxis.** **A.** Example trajectories of wild type *C. elegans* cultivated at 25°C migrating up a linear temperature gradient over a 20-minute period. Top, schematics of the thermal gradient. Middle, trajectories of 49 animals during positive thermotaxis. The starting points of all trajectories are aligned (yellow dot) and the end points are marked by magenta dots. Bottom, a histogram of the final location of animals. **B.** Quantification of the duration of forward run and the angular velocity of run direction as a function of direction of forward run on spatial thermal gradients (top, n=140) and on constant temperature surfaces (bottom, n=140). Error bars are 95% confidence intervals (95% CI). **C.** Thermotaxis trajectory of a single animal during thermotaxis with alternating periods of forward movement and reversals (left), and the instantaneous heading angle over time during one extended period of forward movement within the trajectory (right). Asterisks denote periods where the heading direction pointed down the thermal gradient. **D.** Histogram of temporal changes in temperature ( $dT/dt$ ) experienced by animals during forward runs that ended up pointing up the temperature gradient (n=164).

442 The instantaneous temperature,  $T$ , experienced by the animal is a function of the animal's  
 443 position on the thermal gradient,  $T(t) = c_T P_x(t)$  where  $\vec{P} = \int_0^t \vec{v} d\tau$ .

444 Each simulation is initialized by setting an starting position of (0,0), an initial heading angle  
 445 drawn from the uniform distribution from  $0 - \pm 180^\circ$ , and by setting the animal in a forward run  
 446 state,  $V_2(t_0) = 1$  and  $V_3(t_0) = 1$ . Upon numerical integration, simulated worms move autonomously  
 447 in their environment for a predetermined duration ( $t_{max}$ ).

448 In the behavior simulations used to generate the data shown in **Figure 7**, we have assumed that  
 449 the animal's direction of locomotion does not change during the forward run. This simplification  
 450 is motivated by the observation that RIM ablation specifically disrupts the modulation of run  
 451 duration, while leaving the modulation of run direction intact. Since the latter is likely controlled  
 452 by neural circuitry not modeled here, we chose to focus on the modulation of run duration during  
 453 thermotaxis.

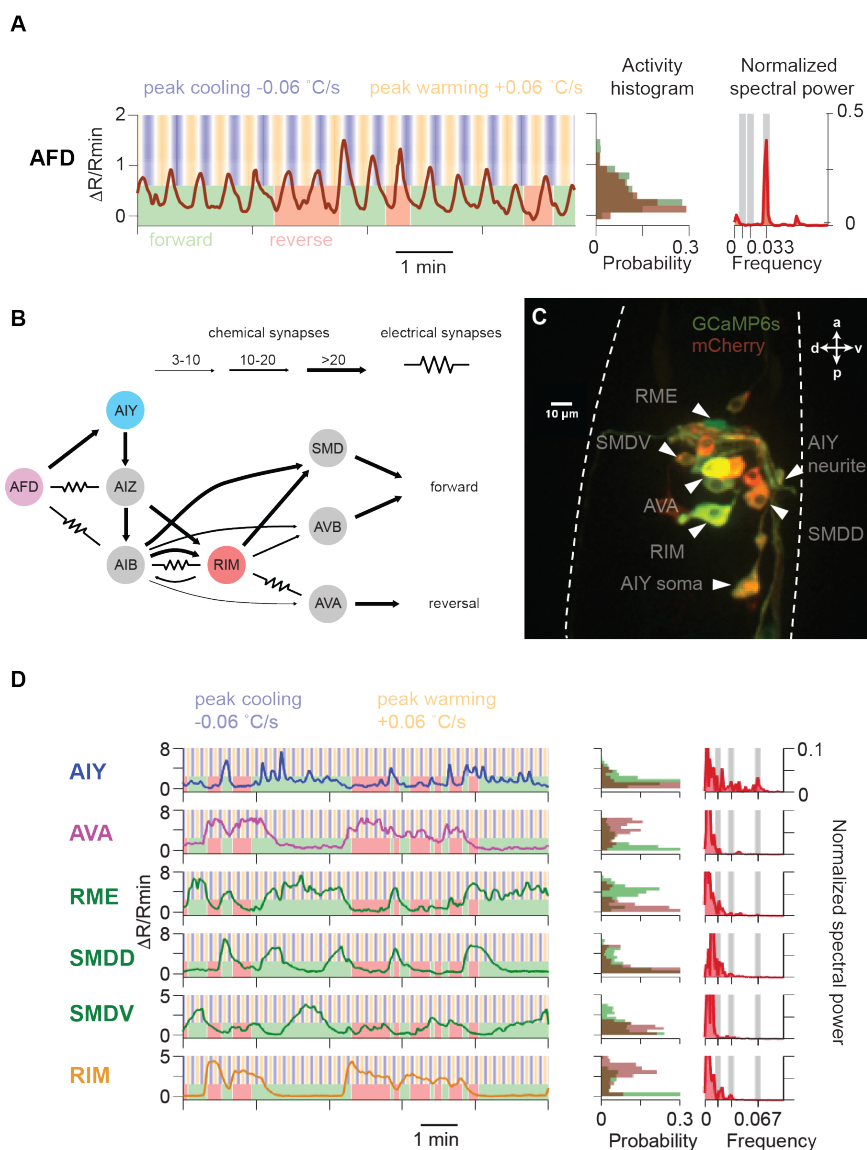


**Figure 2. Neural activity patterns in the thermotactic circuit.** **A.** An example trace of calcium transient of the AFD thermosensory neuron in moving wild type animals in response to an oscillating periodic thermal stimulus at a frequency of  $f_{stim} = 1/30s^{-1}$ . Calcium dynamics overlaid onto the temperature profile and motor state is shown to the left. The histogram and power spectrum of this example trace is shown to the right. Gray bands denote putative oscillation frequencies if the activity of AFD encoded perfectly ( $f_{response} = f_{stim}$ ) or imperfectly ( $f_{response} = 1/2 * f_{stim}$ ,  $1/4 * f_{stim}$ , etc.) the stimulus frequency. **B.** Anatomical connections between AFD, AIY, RIM, and key premotor and motor neurons involved in controlling locomotion during thermotaxis. **C.** Anatomic organization of interneurons and motor neurons implicated in thermotaxis and/or locomotion, denoted by a transgenic strain that expresses the GCaMP6s::wCherry calcium reporter. **D.** Simultaneous measurement of calcium transient changes of neurons downstream of AFD in moving animals responding to a periodic thermal stimulus.

**Figure 2-Figure supplement 1.** Analysis of neural activity in the thermotaxis circuit in immobilized and moving animals without temperature stimulation.

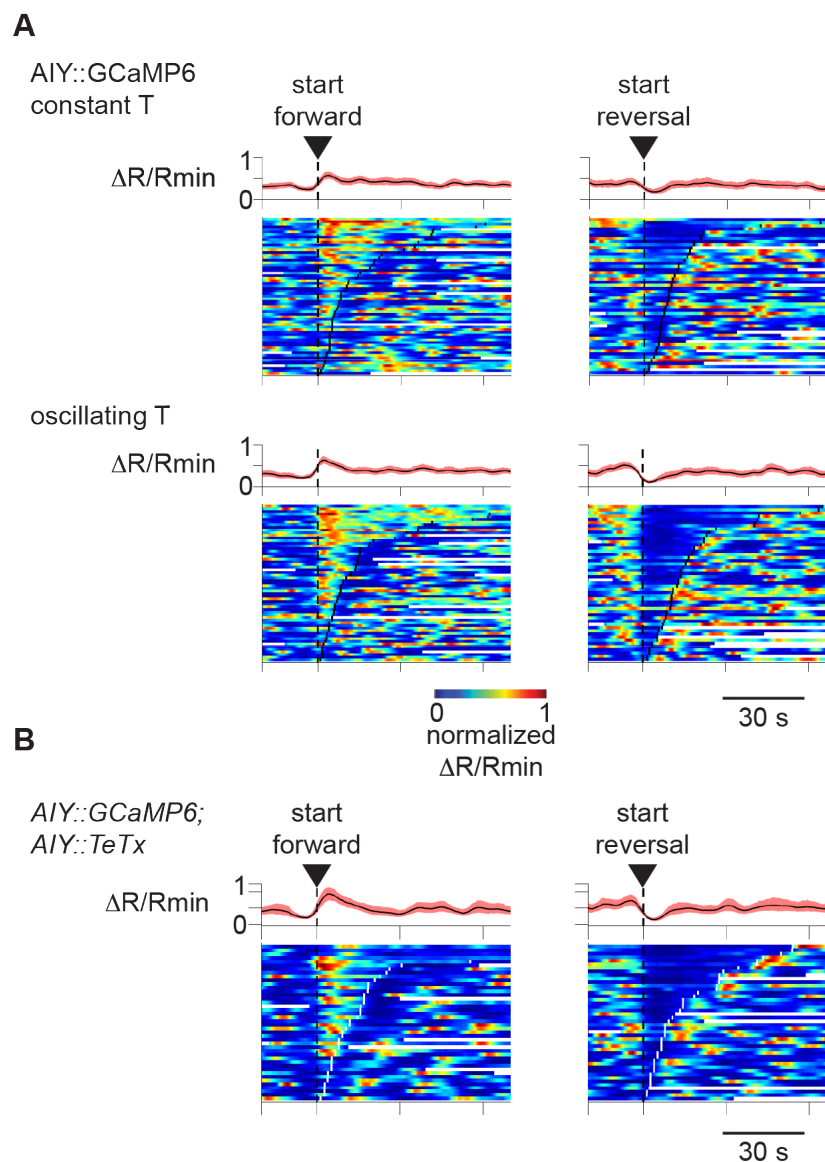


**Figure 3. Motor-related activity in the AIY interneuron represents a CD signal.**

**A.** Traces of calcium transients of the AIY interneuron aligned to the onset of forward runs (left column) or reversals (right column) in animals exposed to oscillating (top row, N = 6 animals) or constant (bottom row, N = 5 animals) temperature. Each row of the heat plots represents changes in AIY calcium transients a single behavioral epoch. The curve on top of each panel represents activity dynamics averaged across individual epochs. Broken black lines denote the onset and offset of individual behavioral epochs. **B.** AIY activity during forward runs and reversals in animals expressing tetanus toxin (TeTx) specifically in AIY at constant temperature (N = 4 animals).

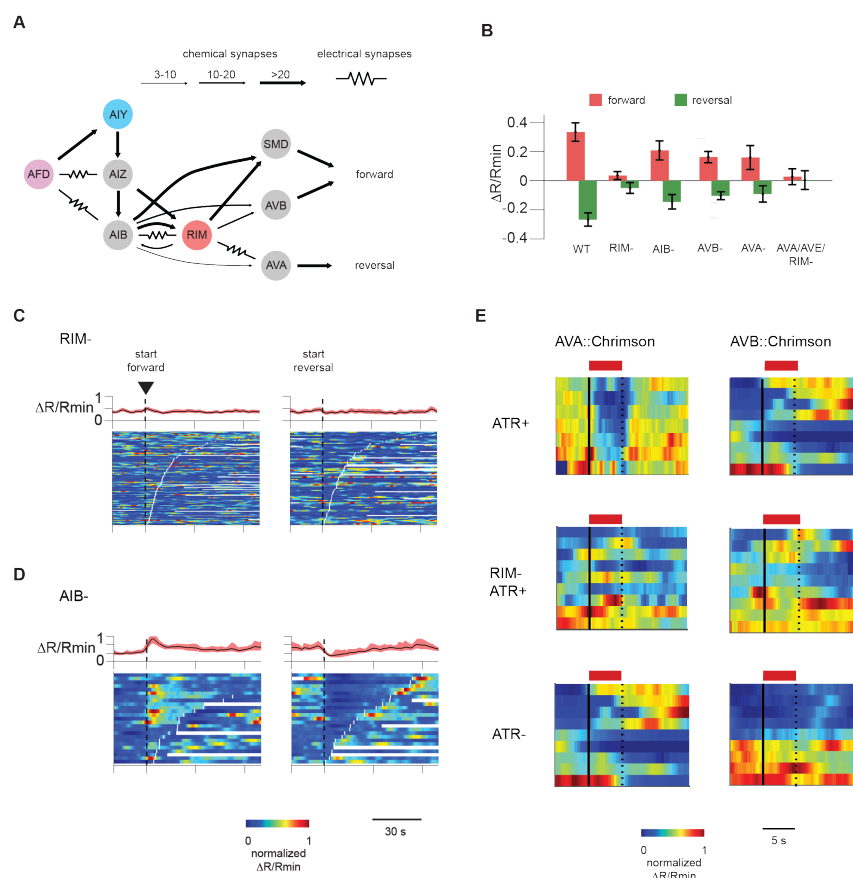


**Figure 4. A CD pathway through the RIM interneuron couples AIY activity with the motor state.**

**A.** Anatomical connections between AFD, AIY, RIM and key premotor and motor neurons involved in controlling locomotion during thermotaxis. **B.** Quantification of motor-related activity in AIY in animals carrying ablations in RIM, AIB, and premotor interneurons. **C.** AIY activity aligned to the onset of forward runs (left) or reversals (right) in animals where RIM has been genetically ablated (N = 8 animals). Each row of the heat maps represent neural activity throughout a single behavioral epoch. The traces on top of the heat plots represent neural activity averaged across individual behavioral epochs. The broken lack lines denote the onset and offset of individual behavioral epochs. **D.** AIY activity aligned to the onset of forward runs (left) or reversals (right) in animals where the AIB interneurons have been genetically ablated (N = 5 animals). **E.** AIY activity in response to optogenetic stimulation of the AVA (left) or AVB (right) premotor interneurons (and others) in wild type animals grown on all-trans retinal (ATR) (top; N = 2 animals for AVA, N = 5 animals for AVB), RIM ablated animals grown on ATR (middle; N = 5 animals for AVA, N = 6 animals for AVB), and wild type animals grown without ATR (bottom, N = 5 animals for AVA, N = 3 animals for AVB).

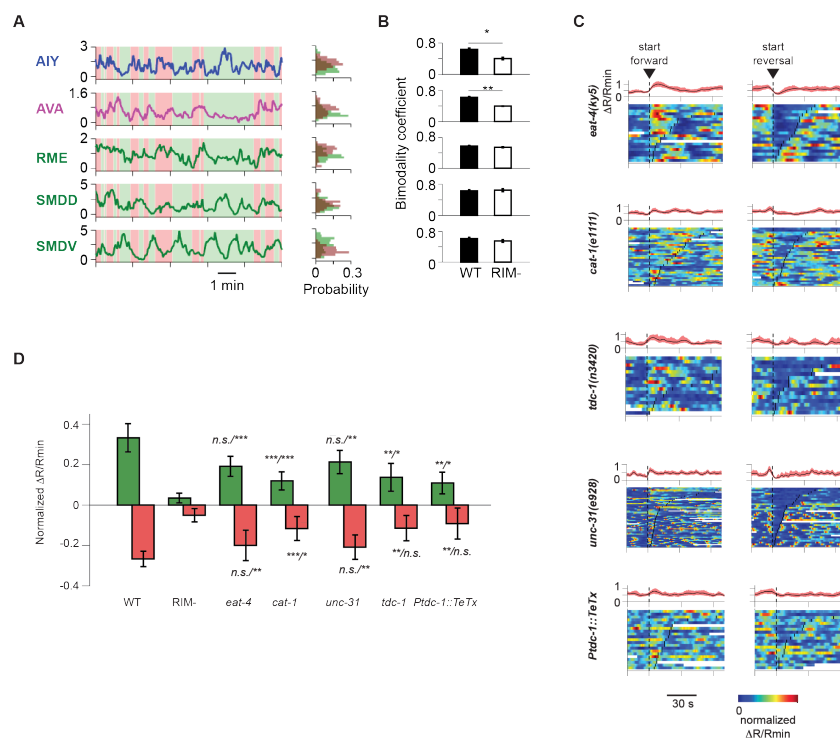


**Figure 5. Loss of RIM eliminates motor state encoding in AIY.** **A.** Simultaneous measurement of calcium transient changes in AIY and neurons of the motor circuit in RIM ablated animals under constant temperature. Sample traces are shown to the left. Activity distribution for each neuron is shown to the right. **B.** Comparison of bi modality coefficients for the activity of individual neurons in wild type versus RIM ablated animals. **C.** AIY activity in *VGLUT3/eat-4(ky5)* mutants (N = 3 animals); *VAMT/cat-1(e1111)* mutants (N = 3 animals); *CAPS/unc-31(e69)* mutants (N = 3 animals); *TDC/tdc-1(n3420)* mutants (N = 4 animals); and in the transgenic animals expressing TeTx (tetanus toxin) specifically in the RIM and RIC neurons (N = 4 animals). **D.** Quantification of motor state activity in AIY in mutants and transgenic animals in (C). Significance of difference in mean between wild type (left) and RIM ablated (right) animals are presented on top of each bar. Error bars are 95% CI. n.s., non-significant, \*,  $p < 0.05$ , \*\*,  $p < 0.01$ , \*\*\*,  $p < 0.001$  by Wilcoxon rank-sum test.

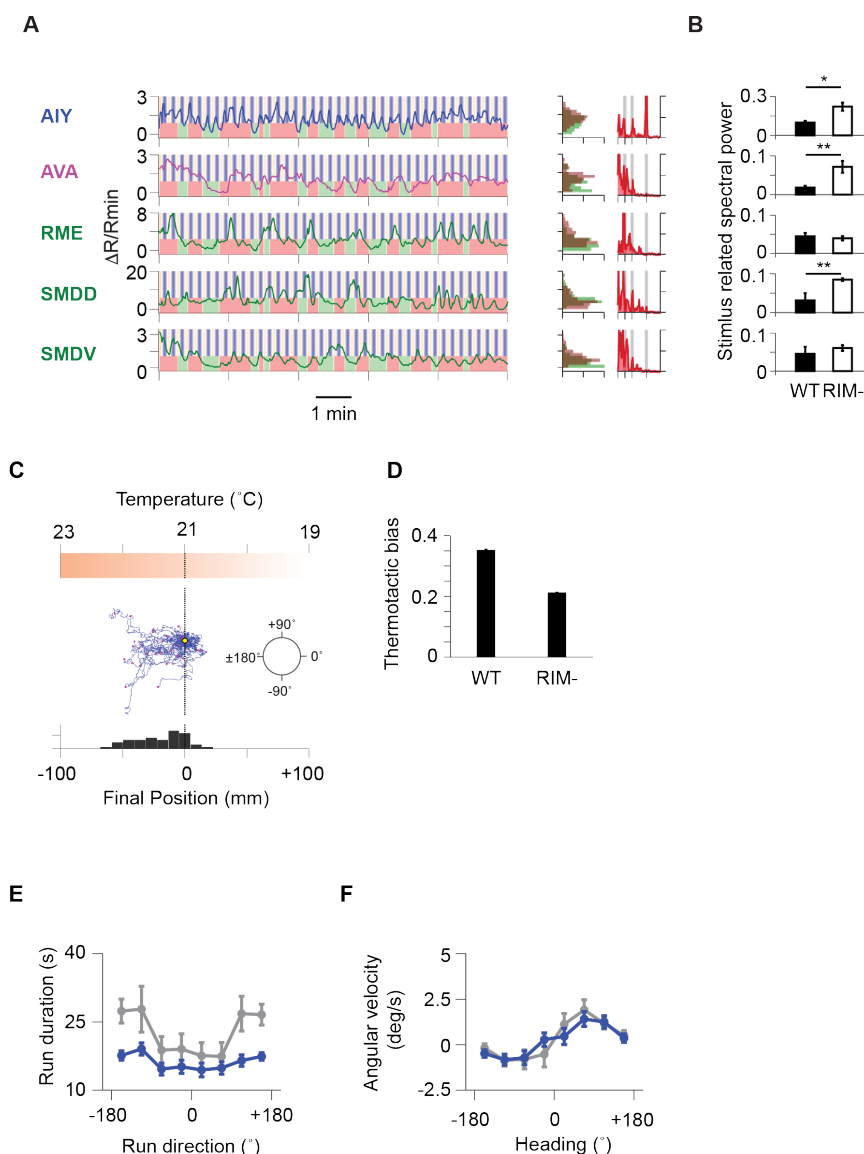


**Figure 6. Loss of RIM leads to defects in positive thermotaxis by eliminating CD to AIY.** **A.** Simultaneous measurement of neural activity in AIY and neurons of the motor circuit (AVA, RME, SMDD/V) in RIM ablated animals under oscillating temperature. Sample traces are shown to the left. The distribution and power spectrum of the calcium activity of individual neurons are shown to the right. Gray bands denote the stimulus frequency. **B.** Comparison of stimulus-related power spectral between wild type and RIM ablated animals (N = 8 for wild type, N = 6 for RIM ablated animals). Error bars are s.e.m. **C.** Example trajectories of RIM ablated animals (N = 39) cultivated at 25 $^{\circ}C$  and exposed to the same thermal gradient as in **Figure 1**. Top, schematics of the thermal gradient. Middle, trajectories of individual animals during positive thermotaxis. Starting points of all trajectories are aligned (yellow dot); the end points are marked by magenta dots. Bottom, a histogram of the final location of animals at the end of the 20-minute period. **D.** Averaged thermotactic bias of wild type (N = 140) and RIM ablated animals (N = 102). **E.** Forward run duration as a function of forward run direction in RIM ablated animals (blue) and wild type animals (gray) during thermotaxis. Error bars are 95% CI. n.s., non-significant, \*, p<0.05, \*\*, p<0.01, \*\*\*, p<0.001 by Wilcoxon rank-sum test. **F.** Instantaneous angular velocity as a function of the instantaneous heading direction in RIM ablated animals (blue) and wild type animals (gray) during thermotaxis. (N = 102).

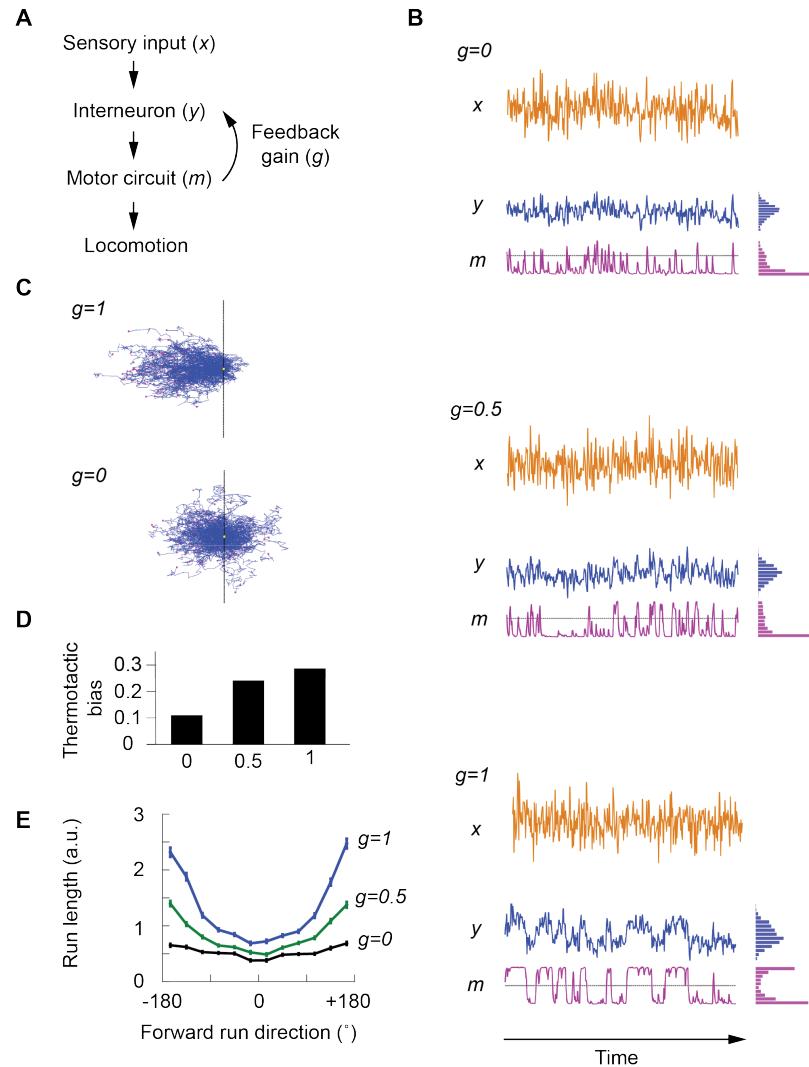


**Figure 7. A reduced model explains the role of CD in sustaining forward locomotion during thermotaxis.** **A.** Schematics of the circuit model. **B.** Dynamics of the model in response to white noise inputs. Top, temporal profile of the input signal. Middle, dynamics of the model with the strength of CD set to 1. Bottom, dynamics of the model with the strength of CD set to 0. **C.** Simulated trajectories of navigational behavior on a 2-D arena with linear input gradient with CD strength set to 0 or 1. **D.** Thermotactic biases of simulations with different CD strengths. **E.** Forward run duration as a function of forward run direction for simulated trajectories

## Acknowledgements

We thank Daniel Witvliet for insights on *C. elegans* connectomes and generating Figures 2B and 4A. We thank the laboratories of Yun Zhang, Daniel Colón-Ramos, and Cori Bargmann for strains. This work was supported by NIH P01 GM103770 (ADTS), NIH R01 NS082525-01A1 (ADTS, MZ, MJA), NIH R01 GM084491 (MJA), the Burroughs Wellcome (VV), and the CIHR foundation 154274 (MZ). We thank Steven Flavell and members of the Samuel, Alkema, and Zhen laboratories for constructive advice and help in completion of the study and manuscript preparation.

## References

- Aivazian D, Serrano RL, Pfeffer S. TIP47 is a key effector for Rab9 localization. *The Journal of Cell Biology*. 2006; 173(6):917–926. <http://jcb.rupress.org/content/173/6/917>, doi: <http://dx.doi.org/10.1083/jcb.200510010>.
- Aksay E, Olasagasti I, Mensh BD, Baker R, Goldman MS, Tank DW. Functional dissection of circuitry in a neural integrator. *Nature neuroscience*. 2007 apr; 10(4):494–504.
- Alkema MJ, Hunter-Ensor M, Ringstad N, Horvitz HR. Tyramine functions independently of octopamine in the *Caenorhabditis elegans* nervous system. *Neuron*. 2005 apr; 46(2):247–260. doi: [10.1016/j.neuron.2005.02.024](https://doi.org/10.1016/j.neuron.2005.02.024).
- Bidaye SS, Machacek C, Wu Y, Dickson BJ. Neuronal Control of *Drosophila*. *Science*. 2014; 344(April):97–101. doi: [10.1126/science.1249964](https://doi.org/10.1126/science.1249964).
- Bloss CS, Wineinger NE, Peters M, Boeldt DL, Ariniello L, Kim JY, Sheard J, Komatireddy R, Barrett P, Topol EJ. A prospective randomized trial examining health care utilization in individuals using multiple smartphone-enabled biosensors. *bioRxiv*. 2016; <http://biorxiv.org/content/early/2016/01/14/029983>, doi: <http://dx.doi.org/10.1101/029983>.
- Brettar I, Christen R, Höfle MG. *Aquiflexum balticum* gen. nov., sp. nov., a novel marine bacterium of the Cytophaga–Flavobacterium–Bacteroides group isolated from surface water of the central Baltic Sea. *International Journal of Systematic and Evolutionary Microbiology*. 2004; 54(6):2335–2341. <http://ijs.microbiologyresearch.org/content/journal/ijsem/10.1099/ijms.0.63255-0>.
- Brettar I, Christen R, Höfle MG. *Belliella baltica* gen. nov., sp. nov., a novel marine bacterium of the Cytophaga–Flavobacterium–Bacteroides group isolated from surface water of the central Baltic Sea. *International Journal of Systematic and Evolutionary Microbiology*. 2004; 54(1):65–70. <http://ijs.microbiologyresearch.org/content/journal/ijsem/10.1099/ijms.0.02752-0>.
- Chalasani SH, Chronis N, Tsunozaki M, Gray JM, Ramot D, Goodman MB, Bargmann CI. Dissecting a circuit for olfactory behaviour in *Caenorhabditis elegans* Gene-specific control of inflammation by TLR-induced chromatin modifications. *Nature*. 2008 nov; 451(January):6540–6540. doi: [10.1038/nature06540](https://doi.org/10.1038/nature06540).
- Chalfie M, Sulston JE, White JG, Southgate E, Thomson JN, Brenner S. The neural circuit for touch sensitivity in *Caenorhabditis elegans*. *Journal of Neuroscience*. 1985 apr; 5(4):956–964. doi: [10.1523/jneurosci.05-04-00956.1985](https://doi.org/10.1523/jneurosci.05-04-00956.1985).
- Chen TW, Wardill TJ, Sun Y, Pulver SR, Renninger SL, Baohan A, Schreiter ER, Kerr RA, Orger MB, Jayaraman V, Looger LL, Svoboda K, Kim DS. Ultrasensitive fluorescent proteins for imaging neuronal activity. *Nature*. 2013; 499(7458):295–300. doi: [10.1038/nature12354](https://doi.org/10.1038/nature12354).
- Clark DA, Biron D, Sengupta P, Samuel ADT, Clark, Biron D, Sengupta P, Samuel ADT. The AFD sensory neurons encode multiple functions underlying thermotactic behavior in *Caenorhabditis elegans*. *Journal of Neuroscience*. 2006; 26(28):7444–7451. doi: [10.1523/jneurosci.1137-06.2006](https://doi.org/10.1523/jneurosci.1137-06.2006).
- Clark DA, Clark DA, Gabel CV, Gabel CV, Gabel H, Gabel H, Samuel ADT. Temporal Activity Patterns in Thermosensory Neurons of Freely Moving *Caenorhabditis elegans* Encode Spatial Thermal Gradients. *Journal of Neuroscience*. 2007 jun; 27(23):6083–6090. <http://www.jneurosci.org/content/jneuro/27/23/6083.full.pdfhttp://www.ncbi.nlm.nih.gov/pubmed/17553981http://www.jneurosci.org/cgi/doi/10.1523/JNEUROSCI.1032-07.2007>, doi: [10.1523/JNEUROSCI.1032-07.2007](https://doi.org/10.1523/JNEUROSCI.1032-07.2007).
- Ferrée TC, Ferrée F, Lockery SR. Computational Rules for Chemotaxis in the Nematode *C. elegans*; 1999.
- Fu Y, Tucciarone JM, Espinosa JS, Sheng N, Darcy DP, Nicoll RA, Huang ZJ, Stryker MP. A cortical circuit for gain control by behavioral state. *Cell*. 2014 mar; 156(6):1139–1152. doi: [10.1016/j.cell.2014.01.050](https://doi.org/10.1016/j.cell.2014.01.050).

- 503 **Gao S**, Xie L, Kawano T, Po MD, Pirri JK, Guan S, Alkema MJ, Zhen M. The NCA sodium leak channel is required for  
504 persistent motor circuit activity that sustains locomotion. *Nature communications*. 2015 feb; 6:ncomms7323.
- 505 **Gordus A**, Pokala N, Levy S, Flavell SW, Bargmann CI. Feedback from Network States Generates Variability in a  
506 Probabilistic Olfactory Circuit. *Cell*. 2015 mar; .
- 507 **Gray JM**, Hill JJ, Bargmann CI. A circuit for navigation in *Caenorhabditis elegans*. *Proceedings of the*  
508 *National Academy of Sciences of the United States of America*. 2005 mar; 102(9):3184–3191. doi:  
509 [10.1073/pnas.0409009101](https://doi.org/10.1073/pnas.0409009101).
- 510 **Hawk JD**, Calvo AC, Liu P, Almoril-Porras A, Aljobeh A, Torruella-Suárez ML, Ren I, Cook N, Greenwood J, Luo  
511 L, Wang ZWW, Samuel ADT, Colón-Ramos DA. Integration of Plasticity Mechanisms within a Single Sensory  
512 Neuron of *C. elegans* Actuates a Memory. *Neuron*. 2018 jan; 97(2):356–367.e4. <http://linkinghub.elsevier.com/retrieve/pii/S0896627317311741>, doi: [10.1016/j.neuron.2017.12.027](https://doi.org/10.1016/j.neuron.2017.12.027).
- 514 **Hedgecock EM**, Russell RL. Normal and mutant thermotaxis in the nematode *Caenorhabditis elegans*. *Proceed-*  
515 *ings of the National Academy of Sciences of the United States of America*. 1975 oct; 72(10):4061–4065. doi:  
516 [10.1073/pnas.72.10.4061](https://doi.org/10.1073/pnas.72.10.4061).
- 517 **Hendricks M**. Compartmentalized calcium dynamics in a *C. elegans* interneuron encode head movement.  
518 *Nature*. 2012 jul; 487(7405):99–103. doi: [10.1038/nature11081](https://doi.org/10.1038/nature11081).
- 519 **Herberholz J**, Antonsen BL, Edwards DH. A lateral excitatory network in the escape circuit of crayfish. *The*  
520 *Journal of Neuroscience*. 2002 oct; 22(20):9078–9085.
- 521 **Hobert O**, Mori I, Yamashita Y, Honda H, Ohshima Y, Liu Y, Ruvkun G. Regulation of interneuron function in the  
522 *C. elegans* thermoregulatory pathway by the *ttx-3* LIM homeobox gene. *Neuron*. 1997 aug; 19(2):345–357.  
523 doi: [10.1016/S0896-6273\(00\)80944-7](https://doi.org/10.1016/S0896-6273(00)80944-7).
- 524 **Hoopfer ED**, Jung Y, Inagaki HK, Rubin GM, Anderson DJ. P1 interneurons promote a persistent internal state that  
525 enhances inter-male aggression in *Drosophila*. *eLife*. 2015; 4(DECEMBER2015):1–27. doi: [10.7554/eLife.11346](https://doi.org/10.7554/eLife.11346).
- 526 **Ino Y**, Yoshida K. Parallel use of two behavioral mechanisms for chemotaxis in *Caenorhabditis elegans*. *Journal*  
527 *of Neuroscience*. 2009 apr; 29(17):5370–5380. doi: [10.1523/JNEUROSCI.3633-08.2009](https://doi.org/10.1523/JNEUROSCI.3633-08.2009).
- 528 **Kato S**, Kaplan HS, Schrödel T, Skora S, Lindsay TH, Yemini E, Lockery S, Zimmer M. Global Brain Dynamics  
529 Embed the Motor Command Sequence of *Caenorhabditis elegans*. *Cell*. 2015 oct; 163(3):656–669. [http://www.](http://www.ncbi.nlm.nih.gov/pubmed/26478179)  
530 [ncbi.nlm.nih.gov/pubmed/26478179](http://www.ncbi.nlm.nih.gov/pubmed/26478179)<http://linkinghub.elsevier.com/retrieve/pii/S0092867415011964>, doi:  
531 [10.1016/j.cell.2015.09.034](https://doi.org/10.1016/j.cell.2015.09.034).
- 532 **Kawano T**, Po MD, Gao S, Leung G, Ryu WS, Zhen M. An imbalancing act: Gap junctions reduce the backward  
533 motor circuit activity to bias *C. elegans* for forward locomotion. *Neuron*. 2011 nov; 72(4):572–586. <http://dx.doi.org/10.1016/j.neuron.2011.09.005>, doi: [10.1016/j.neuron.2011.09.005](https://doi.org/10.1016/j.neuron.2011.09.005).
- 535 **Klappoetke NC**, Murata Y, Kim SS, Pulver SR, Birdsey-Benson A, Cho YK, Morimoto TK, Chuong AS, Carpenter  
536 EJ, Tian Z, Wang J, Xie Y, Yan Z, Zhang Y, Chow BY, Surek B, Melkonian M, Jayaraman V, Constantine-Paton M,  
537 Wong GKS, et al. Independent optical excitation of distinct neural populations. *Nature Methods*. 2014 mar;  
538 11(3):338–346.
- 539 **Kocabas A**, Shen CH, Guo ZV, Ramanathan S. Controlling interneuron activity in *Caenorhabditis elegans* to  
540 evoke chemotactic behaviour. *Nature*. 2012 oct; 490(7419):273–277. doi: [10.1038/nature11431](https://doi.org/10.1038/nature11431).
- 541 **Lee SH**, Dan Y. Neuromodulation of brain states. *Neuron*. 2012 oct; 76(1):209–222.
- 542 **Li WC**, Soffe SR, Wolf E, Roberts A. Persistent responses to brief stimuli: feedback excitation among brainstem  
543 neurons. *The Journal of Neuroscience*. 2006 apr; 26(15):4026–4035.
- 544 **Li Z**, Liu J, Zheng M, Xu XZS. Encoding of both analog- and digital-like behavioral outputs by one *C. Elegans*  
545 interneuron. *Cell*. 2014 nov; 159(4):751–765. doi: [10.1016/j.cell.2014.09.056](https://doi.org/10.1016/j.cell.2014.09.056).
- 546 **Lim MA**, Chitturi J, Laskova V, Meng J, Findeis D, Wiekenberg A, Mulcahy B, Luo L, Li Y, Lu Y, Hung W,  
547 Qu Y, Ho CY, Holmyard D, Ji N, McWhirter R, Samuel ADT, Miller DM, Schnabel R, Calarco JA, et al.  
548 Neuroendocrine modulation sustains the *C. elegans* forward motor state. *eLife*. 2016 nov; 5(NOVEM-  
549 BER2016). <http://elifesciences.org/lookup/doi/10.7554/eLife.19887><https://elifesciences.org/content/5/e19887>,  
550 doi: [10.7554/eLife.19887](https://doi.org/10.7554/eLife.19887).

- 551 **Luo L**, Cook N, Venkatachalam V, Martinez-Velazquez LA, Zhang X, Calvo AC, Hawk J, MacInnis BL, Frank M, Ng  
552 JHR, Klein M, Gershow M, Hammarlund M, Goodman MB, Colon-Ramos DA, Zhang Y, Samuel ADT, Colón-  
553 Ramos DA, Zhang Y, Samuel ADT, et al. Bidirectional thermotaxis in *Caenorhabditis elegans* is mediated by  
554 distinct sensorimotor strategies driven by the AFD thermosensory neurons. *Proceedings of the National*  
555 *Academy of Sciences*. 2014 feb; 111(7):2776–2781. <http://www.pnas.org/cgi/doi/10.1073/pnas.1315205111>,  
556 doi: [10.1073/pnas.1315205111](https://doi.org/10.1073/pnas.1315205111).
- 557 **Luo L**, Wen Q, Ren J, Hendricks M, Gershow M, Qin Y, Greenwood J, Soucy ER, Klein M, Smith-Parker HK, Calvo  
558 AC, Colón-Ramos DA, Samuel ADT, Zhang Y, Colon-Ramos D, Samuel ADT, Zhang Y, Colón-Ramos DA, Samuel  
559 ADT, Zhang Y, et al. Dynamic encoding of perception, memory, and movement in a *C. elegans* chemotaxis  
560 circuit. *Neuron*. 2014; 82(5):1115–1128. doi: [10.1016/j.neuron.2014.05.010](https://doi.org/10.1016/j.neuron.2014.05.010).
- 561 **Major G**, Tank D. Persistent neural activity: prevalence and mechanisms. *Current opinion in neurobiology*. 2004  
562 dec; 14(6):675–684.
- 563 **McCormick KE**, Gaertner BE, Sottile M, Phillips PC, Lockery SR. Microfluidic Devices for Analysis of Spatial  
564 Orientation Behaviors in Semi-Restrained *Caenorhabditis elegans*. *PLoS one*. 2011 oct; 6(10):e25710.
- 565 **McQuilton P**, St Pierre SE, Thurmond J, the FlyBase Consortium. FlyBase 101 – the basics of navigating FlyBase.  
566 *Nucleic Acids Research*. 2012; 40(D1):D706–D714. <http://nar.oxfordjournals.org/content/40/D1/D706.abstract>,  
567 doi: <http://dx.doi.org/10.1093/nar/gkr1030>.
- 568 **Mori I**, Ohshima Y. Neural regulation of thermotaxis in *Caenorhabditis elegans*. *Nature*. 1995 jul; 376(6538):344–  
569 348. doi: [10.1038/376344a0](https://doi.org/10.1038/376344a0).
- 570 **Narayan A**, Laurent G, Sternberg PW. Transfer characteristics of a thermosensory synapse in *Caenorhabditis*  
571 *elegans*. *Proceedings of the National Academy of Sciences of the United States of America*. 2011 jun;  
572 108(23):9667–9672. doi: [10.1073/pnas.1106617108](https://doi.org/10.1073/pnas.1106617108).
- 573 **Ouellette MH**, Desrochers MJ, Gheta I, Ramos R, Hendricks M. A Gate-and-Switch Model for Head Orientation  
574 Behaviors in *Caenorhabditis elegans*. *ENEURO*. 2018; 5(6):ENEURO.0121–18.2018. doi: [10.1523/eneuro.0121-18.2018](https://doi.org/10.1523/eneuro.0121-18.2018).
- 575
- 576 **Petreaanu L**, Mao T, Sternson SM, Svoboda K. The subcellular organization of neocortical excitatory connections.  
577 *Nature*. 2009 jan; 457(7233):1142–1145. doi: [10.1038/nature07709](https://doi.org/10.1038/nature07709).
- 578 **Pfister R**, Schwarz K, Janczyk M, Dale R, Freeman J. Good things peak in pairs: a note on the bimodality coefficient.  
579 *Frontiers in Psychology*. 2013; 4:700. <https://www.frontiersin.org/article/10.3389/fpsyg.2013.00700>, doi:  
580 [10.3389/fpsyg.2013.00700](https://doi.org/10.3389/fpsyg.2013.00700).
- 581 **Pierce-Shimomura JT**, Morse TM, Lockery SR, Lockery SR. The fundamental role of pirouettes in *Caenorhabditis*  
582 *elegans* chemotaxis. *The Journal of Neuroscience*. 1999 nov; 19(21):9557–9569.
- 583 **Qi YB**, Garren EJ, Shu X, Tsien RY, Jin Y. Photo-inducible cell ablation in *Caenorhabditis elegans* using the  
584 genetically encoded singlet oxygen generating protein miniSOG. *Proceedings of the National Academy of*  
585 *Sciences of the United States of America*. 2012 may; 109(19):7499–7504. doi: [10.1073/pnas.1204096109](https://doi.org/10.1073/pnas.1204096109).
- 586 **Ryu WS**, Samuel ADT. Thermotaxis in *Caenorhabditis elegans* analyzed by measuring responses to defined  
587 Thermal stimuli. *The Journal of Neuroscience*. 2002 jul; 22(13):5727–5733.
- 588 **Schneider DM**, Nelson A, Mooney R. A synaptic and circuit basis for corollary discharge in the auditory cortex.  
589 *Nature*. 2014 sep; 513(7517):189–194. doi: [10.1038/nature13724](https://doi.org/10.1038/nature13724).
- 590 **Seelig JD**, Jayaraman V. Neural dynamics for landmark orientation and angular path integration. *Nature*. 2015  
591 may; 521(7551):186–191. doi: [10.1038/nature14446](https://doi.org/10.1038/nature14446).
- 592 **Serrano-Saiz E**, Poole RJ, Felton T, Zhang F, De La Cruz ED, Hobert O. XModular control of glutamater-  
593 gic neuronal identity in *C. elegans* by distinct homeodomain proteins. *Cell*. 2013 oct; 155(3):659. doi:  
594 [10.1016/j.cell.2013.09.052](https://doi.org/10.1016/j.cell.2013.09.052).
- 595 **Seung HS**. How the brain keeps the eyes still. *Proceedings of the National Academy of Sciences*. 1996 nov;  
596 93(23):13339–13344.
- 597 **Shen Y**, Wen Q, Liu H, Zhong C, Qin Y, Harris G, Kawano T, Wu M, Xu T, Samuel ADT, Zhang Y. An extrasynap-  
598 tic GABAergic signal modulates a pattern of forward movement in *Caenorhabditis elegans*. *eLife*. 2016;  
599 5(MAY2016):e14197. <http://dx.doi.org/10.7554/eLife.14197>, doi: [10.7554/eLife.14197](https://doi.org/10.7554/eLife.14197).

- 600 **Shu X**, Lev-Ram V, Deerinck TJ, Qi Y, Ramko EB, Davidson MW, Jin Y, Ellisman MH, Tsien RY. A Genetically Encoded  
601 Tag for Correlated Light and Electron Microscopy of Intact Cells, Tissues, and Organisms. *PLoS biology*. 2011  
602 apr; 9(4):e1001041.
- 603 **Tsalik EL**, Hobert O. Functional mapping of neurons that control locomotory behavior in *Caenorhabditis elegans*.  
604 *Journal of Neurobiology*. 2003 jun; 56(2):178–197. doi: [10.1002/neu.10245](https://doi.org/10.1002/neu.10245).
- 605 **Wakabayashi T**, Kitagawa I, Shingai R. Neurons regulating the duration of forward locomotion in *Caenorhabditis*  
606 *elegans*. *Neuroscience Research*. 2004 sep; 50(1):103–111. doi: [10.1016/j.neures.2004.06.005](https://doi.org/10.1016/j.neures.2004.06.005).
- 607 **Ward S**. Chemotaxis by the nematode *Caenorhabditis elegans*: identification of attractants and analysis of  
608 the response by use of mutants. *Proceedings of the National Academy of Sciences of the United States of*  
609 *America*. 1973 mar; 70(3):817–821. doi: [10.1073/pnas.70.3.817](https://doi.org/10.1073/pnas.70.3.817).
- 610 **White JG**, Southgate E, Thomson JN, Brenner S. The Structure of the Nervous System of the Nematode  
611 *Caenorhabditis elegans*. *Philosophical Transactions of the Royal Society B: Biological Sciences*. 1986;  
612 314(1165):1–340. doi: [10.1098/rstb.1986.0056](https://doi.org/10.1098/rstb.1986.0056).
- 613 **Yamaguchi S**, Naoki H, Ikeda M, Tsukada Y, Nakano S, Mori I, Ishii S. Identification of animal behavioral strategies  
614 by inverse reinforcement learning. *PLoS Computational Biology*. 2018; 14(5):1–20. [http://dx.doi.org/10.1371/](http://dx.doi.org/10.1371/journal.pcbi.1006122)  
615 [journal.pcbi.1006122](http://dx.doi.org/10.1371/journal.pcbi.1006122), doi: [10.1371/journal.pcbi.1006122](https://doi.org/10.1371/journal.pcbi.1006122).
- 616 **Zagha E**, Casale AE, Sachdev RNS, McGinley MJ, McCormick DA. Motor cortex feedback influences sensory pro-  
617 cessing by modulating network state. *Neuron*. 2013 aug; 79(3):567–578. doi: [10.1016/j.neuron.2013.06.008](https://doi.org/10.1016/j.neuron.2013.06.008).
- 618 **Zhang Y**, Lu H, Bargmann CI. Pathogenic bacteria induce aversive olfactory learning in *Caenorhabditis elegans*. .  
619 2005 nov; 438(7065):179–184.

620 **Appendix 1**

621 **Constructs and transgenic arrays**

<b>Calcium imaging</b>			
<b>Plasmid</b>	<b>Injection Marker</b>	<b>Transgene</b>	<b>Strain</b>
pDACR1286[ <i>Pmod-1::GCaMP6s</i> ] (25ng/μl); pDACR63[ <i>Pttx-3::mCherry</i> ] (25ng/μl)	pDACR218[ <i>Punc-122::dsRed</i> ] (40ng/μl)	<i>aeals003(AIY)</i> ( <i>integrated olaEx1621<sup>a</sup></i> )	ADS003
pDACR943[ <i>Pgcy-8::GCaMP6s</i> ] (30ng/μl); pDACR801 [ <i>Pgcy-8::mCherry</i> ] (5ng/μl)	pDACR20[ <i>Punc122::GFP</i> ] (20ng/μl)	<i>aeals004 (AFD)</i> ( <i>integrated olaEx1527<sup>b</sup></i> )	ADS004
pJH3338[ <i>Pglr-1-GCaMP6s::wCherry</i> ]	pL15EK[ <i>lin-15AB genomic DNA</i> ] (20ng/μl)	<i>hpls471</i> ( <i>premotor/ motor</i> )	ZM8558
<b>Optogenetic stimulation</b>			
pHR2[ <i>P<sub>lgc-55B-Chrimson</sub>::wCherry</i> ]	pL15EK[ <i>lin-15AB genomic DNA</i> ] (80ng/μl)	<i>aeaEx003 (AVB/others)</i>	ADS029
pHR6[ <i>Prig-3-Chrimson::wCherry</i> ]	pL15EK[ <i>lin-15AB genomic DNA</i> ] (80ng/μl)	<i>aeaEx005 (AVA/others)</i>	ADS031
<b>Cell ablation</b>			
pJH2829[ <i>Pcex-1- MiniSOG::SL2::wCherry</i> ]	pL15EK[ <i>lin-15AB genomic DNA</i> ] (20ng/μl)	<i>hpls327 (RIM)</i>	ZM7978
pJH3311[ <i>Pinx-1- MiniSOG::SL2::wCherry</i> ]	pL15EK[ <i>lin-15AB genomic DNA</i> ] (20ng/μl)	<i>hpls465(AIB)</i>	ZM8484
pJH2931[ <i>Prig-3- MiniSOG::SL2::wCherry</i> ]	pL15EK[ <i>lin-15AB genomic DNA</i> ] (20ng/μl)	<i>hpEx3072 (AVA/others)</i>	ZM7198
pJH2890[ <i>P<sub>lgc-55B- MiniSOG</sub>::SL2::wCherry</i> ]	pL15EK[ <i>lin-15AB genomic DNA</i> ] (20ng/μl)	<i>hpls331(AVB/others)</i>	ZM7297
pJH2890[ <i>Pnmr-1-MiniSOG::SL2::wCherry</i> ]	pL15EK[ <i>lin-15AB genomic DNA</i> ] (20ng/μl)	<i>hpls321(AVA/E/D/RIM/PVC/others)</i>	ZM7054
<b>Synaptic manipulation</b>			
<i>Pttx-3::TeTx::mCherry<sup>c</sup></i>		<i>yxIs25 (AIY)</i>	ZC1952
<i>Ptdc-1::TeTx::mCherry<sup>d</sup></i>		<i>kyEx4962 (RIM/RIC)</i>	CX14993

<sup>a</sup>Gift of Daniel Colon-Ramos

<sup>b</sup>Gift of Daniel Colon-Ramos

<sup>c</sup>Zhang et al. (2005)

<sup>d</sup>Gordus et al. (2015)

623 **Appendix 2**

624 **Strains**

<b>For thermotaxis and locomotion assays</b>			
<b>Strain</b>	<b>Genotype</b>	<b>Purpose</b>	<b>Figure</b>
Bristol N2	wild-type	Wild-type behavior	<i>Figure 1A-D</i>
ZM7978	<i>hpls327</i>	Behavior upon RIM ablation	<i>Figure 6C-F</i>
<b>Calcium imaging</b>			
ADS003	<i>aeals003</i>	AIY imaging	<i>Figure 2D;3A,B</i>
ADS004	<i>aeals004</i>	AFD imaging	<i>Figure 2A</i>
ADS027	<i>aeals003; hpls471</i>	Simultaneous imaging of AIY, AVA, RME, SMDD, SMDV and RIM	<i>Figure 2C,D</i>
ADS043	<i>aeals003; yxls25</i>	AIY imaging, upon blockade of AIY chemical transmission	<i>Figure 3B</i>
ADS010	<i>aeals003; hpls327</i>	AIY imaging, upon ablation of RIM	<i>Figure 4B,C;5A,B,D;6A,B</i>
ADS014	<i>aeals003; hpls321</i>	AIY imaging, upon ablation of RIM, AVA, AVE, AVD and PVC	<i>Figure 4B</i>
ADS026	<i>aeals003; hpEx3072</i>	AIY imaging upon ablation of AVA	<i>Figure 4B</i>
ADS036	<i>aeals003; hpls331</i>	AIY imaging, upon ablation of AVB	<i>Figure 4B</i>
ADS046	<i>aeals003; hpls465</i>	AIY imaging, upon ablation of AIB	<i>Figure 4B,D</i>
ADS029	<i>aeaEx003; aeals003; lite-1(ce314)</i>	AIY imaging upon optogenetic stimulation of AVB	<i>Figure 4E</i>
ADS031	<i>aeaEx005; aeals003; lite-1(ce314)</i>	AIY imaging upon optogenetic stimulation of AVA	<i>Figure 4E</i>
ADS033	<i>aeaEx005; aeals003; hpls327; lite-1(ce314)</i>	AIY imaging, upon RIM ablation and AVA stimulation	<i>Figure 4E</i>
ADS035	<i>aeaEx003; aeals003; hpls327; lite-1(ce314)</i>	AIY imaging, upon RIM ablation and AVB stimulation	<i>Figure 4E</i>
ADS013	<i>aeals003; kyEx4962</i>	AIY imaging, upon disruption of RIM/RIC chemical transmission	<i>Figure 5C,D</i>
ADS006	<i>aeals003; tdc-1(n3419)</i>	AIY imaging in tyramine/octopamine synthesis mutant	<i>Figure 5C,D</i>
QW1411	<i>aeals003; eat-4(ky5)</i>	AIY imaging in glutamate mutant	<i>Figure 5C,D</i>
QW1175	<i>aeals003; unc-31(e928)</i>	AIY imaging in dense core vesicle release mutant	<i>Figure 5C,D</i>
QW1408	<i>aeals003; cat-1(e1111)</i>	AIY imaging in biogenic amine transporter mutant	<i>Figure 5C,D</i>

625

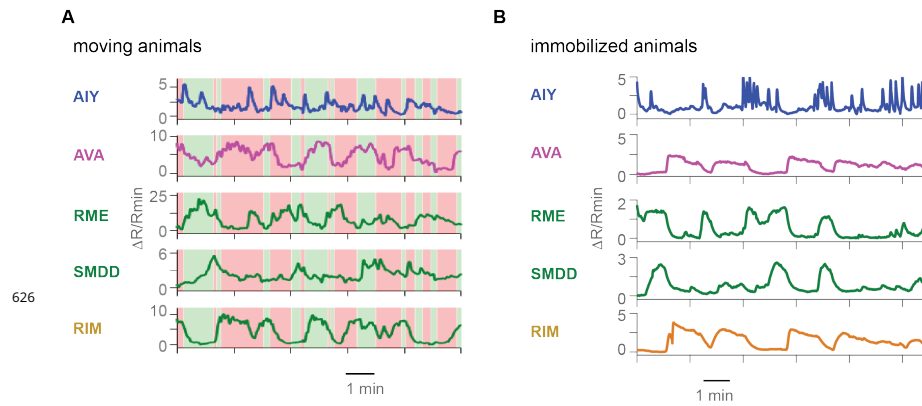


**Figure 2-Figure supplement 1. Analysis of neural activity in the thermotaxis circuit in immobilized and moving animals without temperature stimulation.** **A.** Simultaneous measurement of calcium transient changes of neurons labeled by the transgenic reporter in moving (left) and immobilized (right) animals at constant temperature ( $T = 15^{\circ}\text{C}$ ). **B.** Cross correlation between the activity of RIM and that of other neurons measured in (A) in immobilized and moving animals.